

Supporting Information

Rapid expansion of wetlands on the Central Tibetan Plateau by global warming and El Niño

Yang Li^{1#}, Zhengyang Hou^{1#}, Liqiang Zhang¹, Changqing Song¹, Shilong Piao², Jintai Lin³, Shushi Peng², Keyan Fang⁴, Jing Yang¹, Ying Qu¹, Yuebin Wang¹, Jingwen Li⁵, Roujing Li¹, Xin Yao¹

¹*State Key Laboratory of Remote Sensing Science, Faculty of Geographical Science, Beijing Normal University, Beijing 100875, China*

²*College of Urban and Environmental Sciences, Peking University, 100871, Beijing, China*

³*Laboratory for Climate and Ocean-Atmosphere Studies, Department of Atmospheric and Oceanic Sciences, School of Physics, Peking University, Beijing, 100871, China*

⁴*Key Laboratory of Humid Subtropical Eco-geographical Process (Ministry of Education), College of Geographical Sciences, Fujian Normal University, Fuzhou, China*

⁵*Guangxi Key Laboratory of Spatial Information and Geomatics, Guilin University of Technology, Guangxi, China*

1. Datasets

Landsat images, including Landsat 5 Thematic Mapper (TM) for the 1990s, Landsat 7 Enhanced Thematic Mapper Plus (ETM+) from 2000 to 2012, and Landsat 8 Operational Land Imager (OLI) sensor from 2013 to 2019, were used for wetland extraction. All images were obtained in September and October to reduce the effects of seasonal fluctuations of hydrology on wetland areal extents. For the images of the Landsat 7 ETM+ sensor after 2003, there are wedge-shaped gaps with about 12 pixels towards the edges of the scene due to sensor failure of the Scan Line Corrector [1]. We thus used the inverse distance weight interpolation algorithm to fill in the gaps. We selected six common bands of the three Landsat sensors, including Band1-Band5 and Band7 for TM and ETM+ sensors, and Band2-Band7 for OLI sensors, to classify

1 wetlands.

2 The normalized difference vegetation index (NDVI) and the modified normalized
3 difference water index (mNDWI) were used to acquire the water surface and
4 vegetation-covered area.

5 We obtained the slopes and elevations of the terrains from the digital elevation model
6 data of the Space Shuttle Radar Terrain Mission (SRTM).

7 **Climate data.** We captured the temperature and precipitation data from the daily
8 meteorological dataset of China National Surface Weather Station (V3.0) archived in
9 the National Tibetan Plateau Science Data Center of China (<https://data.tpsc.ac.cn/>).
10 The dataset contains quality-controlled daily values of temperature and precipitation
11 for 84 meteorological stations across the TP since January 1951. We calculated the
12 annual average temperature and precipitation for each TP station from 1990 to 2019.
13 We also used evaporation data from the Global Land Evaporation Amsterdam Model
14 (GLEAM) (www.gleam.eu), which estimated evaporation based on data from weather
15 stations and satellite remote sensing [2,3]. The Sea Surface Temperature (SST) data
16 used in this study were captured from the Met Office Hadley Centre
17 (<http://hadobs.metoffice.gov.uk/hadisst/>).

18 **Ocean Niño Index.** The Ocean Niño Index (ONI, <https://origin.cpc.ncep.noaa.gov/>)
19 is a NOAA's primary indicator for the ocean component of the El Niño-Southern
20 Oscillation (ENSO). The ONI monitors the average sea surface temperatures in the east-
21 central tropical Pacific Ocean between 120°W-170°W for three consecutive months,
22 and whether they are warmer or cooler than the average, which indicates El Niño and
23 La Niña events.

24 **2. Framework for TP wetland extraction**

25 The widely accepted definition of wetlands was formulated by the Ramsar
26 Convention. Wetlands are the areas of marsh, fen, peatland, and water, whether natural
27 or artificial, permanent or temporary, with water that is static or flowing, fresh, brackish
28 or salt. In this study, we mainly extract the following categories of the TP wetlands,
29 namely, lakes (including lake beaches, salt lakes), rivers (including river beaches),
30 vegetated wetlands including moss marshes, herbaceous marshes and inland salt
31 marshes. Other types of wetlands such as forest swamps and coastal wetlands are much
32 less distributed on the TP [4,5], and we omit them in this study.

33 Wetland extraction from remote sensing images is a challenge due to uncertainty of
34 wetland boundaries, complexity of spectral and texture characteristics [6]. Most

1 previous works were based on pixel-based or object-based classification with machine
2 learning models. Here, we present a scene-based classification framework with the deep
3 learning model to precisely classify wetlands. Since increase of the number and
4 diversity of the training data help to enhance the model performance[7], the training
5 samples are composed of two data sources. The first data source was from the existing
6 wetland products as the pre-training samples, including 428,182 positive samples
7 (wetlands) and 351,224 negative samples (non-wetlands). Research Centre (JRC)
8 surface water [8] and national wetland mapping in China from Chinese Academy of
9 Sciences (CAS_Wetlands) [4] were used as the reference to generate the pre-training
10 samples. The second source came from the manually annotated data with the help of
11 very high spatial resolution (VHSR) images from Google Earth. 34,232 visually
12 interpreted wetland samples and the same number of non-wetland samples were
13 generated by visual interpretation. Our deep learning framework inherits the advantage
14 of transfer learning, which guarantees that our pre-trained deep learning model achieves
15 high classification performance using a few samples on the TP[9,10].

16 Fig. S1 illustrates the framework for TP wetland extraction from Landsat images in
17 1990-2019. The data are fed into the deep learning framework based on SE-ResNet-50
18 [11]. To accept multi-modality image inputs, we modified the first layer of SE-ResNet-
19 50. Then, the trained framework was employed to classify wetlands from the images.
20 To obtain pixel-by-pixel wetland boundary and improve wetland classification accuracy,
21 each pixel in the images was traversed for 100 times. The pixel was a wetland point, if
22 there were no less than 85 times for it to be judged as a wetland point.

23 **3. Validations of wetland extraction and quantifying uncertainty**

24 The stratified random sampling method, which is a widely used validation approach
25 for accuracy assessment of land cover classification[12], combined with VHSR images
26 from Google Earth, were used to perform accuracy assessment of wetland extraction.
27 493 wetland samples and 4,145 non-wetland samples are selected according to Eq. (1).

$$28 \quad n = \frac{z^2 p(1-p)}{d^2} \quad (1)$$

29 where $z = 1.96$ for a 95% confidence interval (CI), p is represented as the area
30 proportion for the target wetland class. Here $p=0.088$ since the largest proportion of the
31 extracted wetland area to the TP area is 8.8%. d is the half of the width of the 95% CI,
32 i.e. $d=0.025$.

33 Three metrics i.e. user accuracy (UA), producer accuracy (PA), and F1 score, were

1 used to validate the wetland mapping accuracy. The validations showed the user's
 2 accuracy for wetland extraction was 96.1%, and the producer's accuracy was 90.8%.
 3 The F1 score was 0.934, highlighting a good balance between commission and
 4 omission errors.

5 The standard error of the error-adjusted estimated area with the approximate 95% CI
 6 [13] was used to quantify the uncertainty of the wetland areal extent.

$$7 \quad \hat{A}_j \pm 1.96 \times S(\hat{A}_j) \quad (2)$$

$$8 \quad S(\hat{A}_j) = A_{tot} \times \sqrt{\sum_{i=1}^2 W_i^2 \frac{n_{ij} \left(1 - \frac{n_{ij}}{n_i}\right)}{n_i - 1}} \quad (3)$$

9 where the total area of the TP is A_{tot} , the mapped area of wetland is A_i , and $W_i =$
 10 A_i / A_{tot} . n_{ij} denotes the elements of the i-th row and j-th column in the error
 11 matrix of sample counts. n_i denotes the sum of the i-th row in the error matrix of
 12 sample counts.

13 Considering the propagation of the uncertainty, we use Eq. (4) to obtain the
 14 uncertainty of the wetland changes.

$$15 \quad S(\Delta\hat{A}) = \sqrt{S(\hat{A})^2_{first} + S(\hat{A})^2_{last}} \quad (4)$$

16 **4. Statistical analysis**

17 For each zone on the TP, we first calculated the correlation between the wetland
 18 area changed and individual meteorological factor like the annual average temperature,
 19 precipitation and potential evapotranspiration. To reduce the influence of the inter-
 20 annual data jitter, the moving average of three years for each climatic factor and
 21 wetlands in different regions were taken for the analysis. To further analyze the relative
 22 contributions of each factor, we used a multivariate general linear model [14] for
 23 analysis of variance (ANOVA).

24 To characterize the overall correlation between the TP wetland areal extent and
 25 global sea surface temperature (SST), the cross-covariance matrix of the two fields was
 26 calculated from the correlation matrix of the normalized data. We used the singular
 27 value decomposition (SVD) on the cross-covariance matrix between the TP wetland
 28 areal extent and global sea surface temperature (SST) to explore the coupled
 29 distribution pattern. The SVD is an easily interpreted method to analyze the
 30 relationships between time series of two fields in meteorology [15]. Prior to the SVD,
 31 the wetland areal extent and SST were by the first-differenced process.

1 **5. Extraction of lakes**

2 To examine whether the wetland area increase on Qiangtang Plateau and the source
3 region of Yangtze River caused by permafrost thaw, we extract lake objects on the two
4 zones in five periods (1990-1991, 1996-1997, 2002, 2015 and 2018) from Landsat
5 imagery to find the variations of the lake count and areal extent. The five periods were
6 chosen because the wetlands rapidly grew from 1996 to 2002 for the first time and from
7 2015 to 2018 for the second time since 1990. Due to poor quality of Landsat 5 imagery,
8 results for each of the first two periods (1990-1991 and 1996-1997) were calculated
9 from image data of two years. We selected 356 positive samples and 402 negative
10 samples by manual labeling, and used the Support Vector Machine (SVM) classifier to
11 extract water bodies. Six common bands of TM and OLI images, NDVI and NDWI
12 were inputted to the model. The Google Earth Engine was used to produce a surface
13 water map on Qiangtang Plateau and the source region of Yangtze River. Considering
14 the lakes $< 5,000 \text{ m}^2$ (about 5 pixels) were very difficult to be recognized from Landsat
15 imagery, we omitted the extraction of these lakes and deleted the misidentified lakes.

16

17

1 Figures

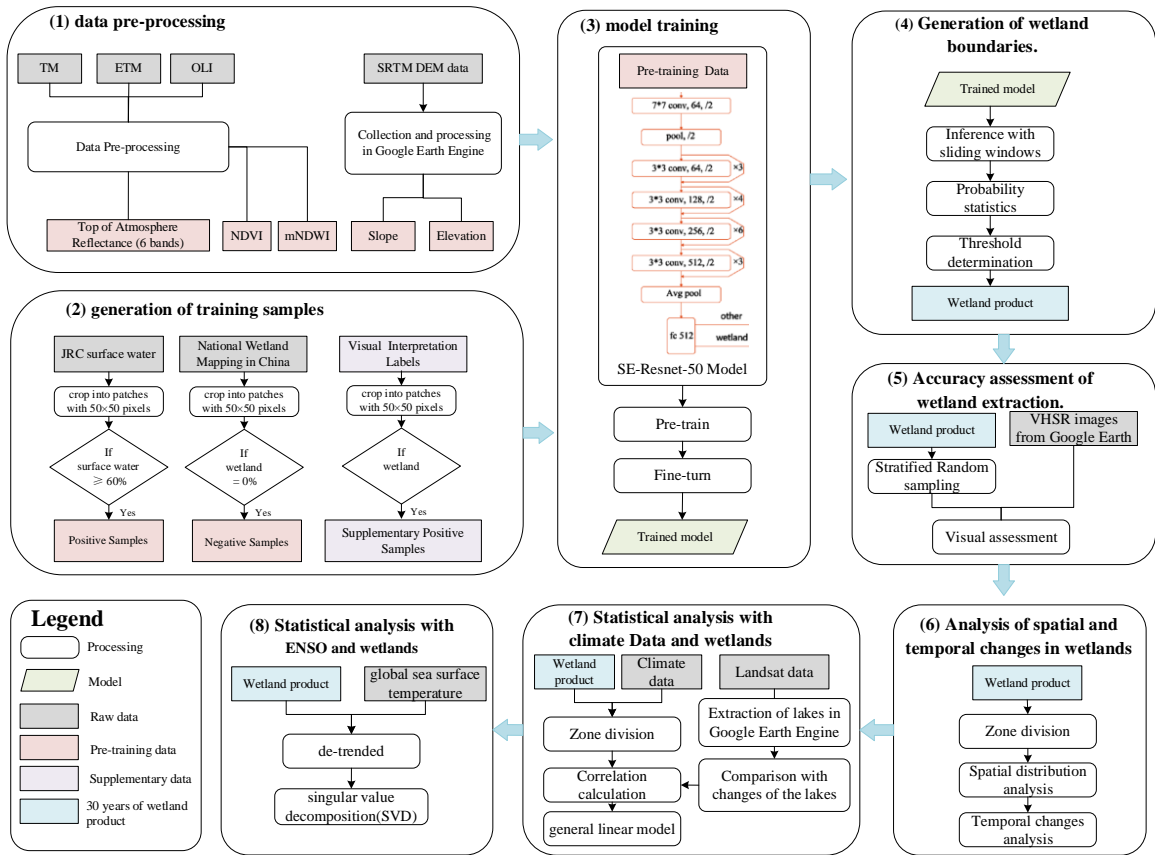
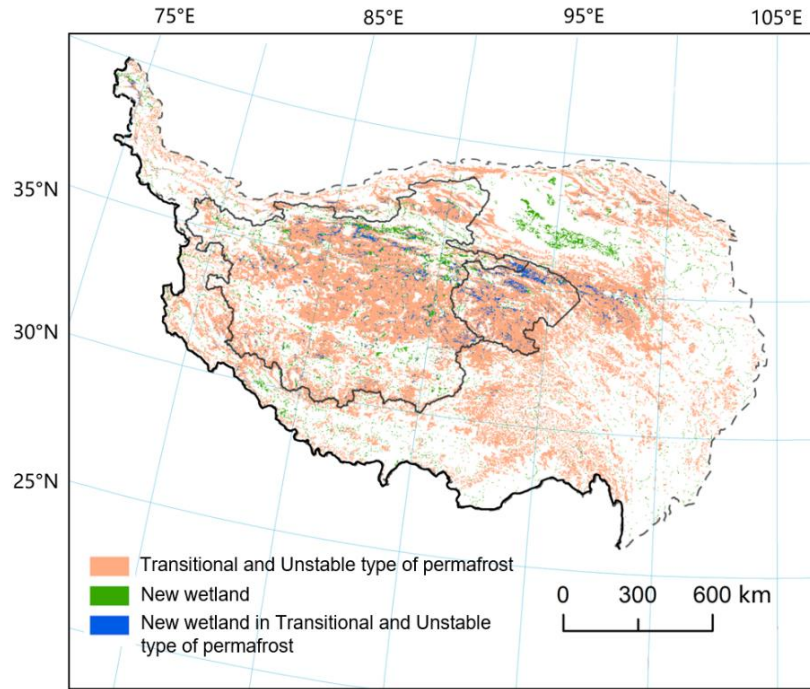


Fig. S1. The framework in this study.

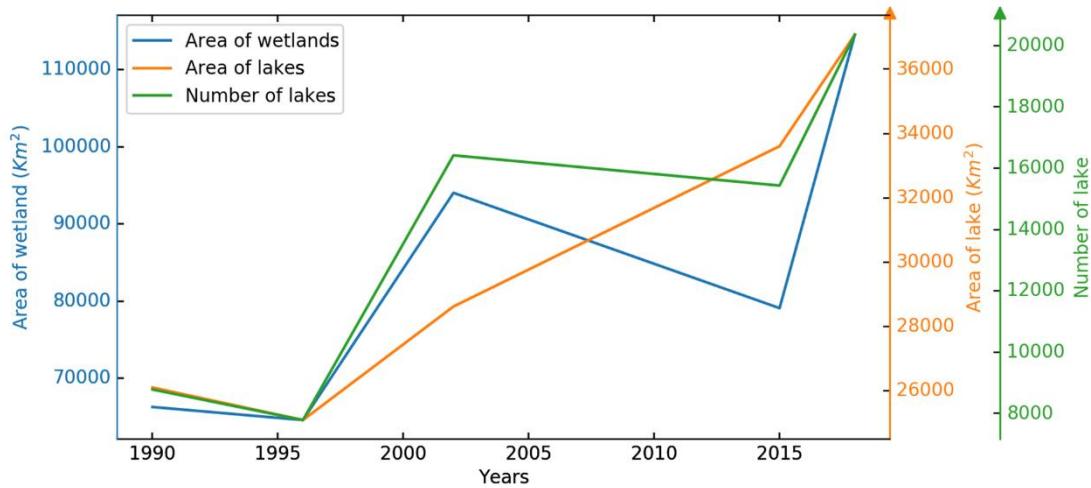
2
3
4
5
6
7
8



审图号: GS京(2023)0108号

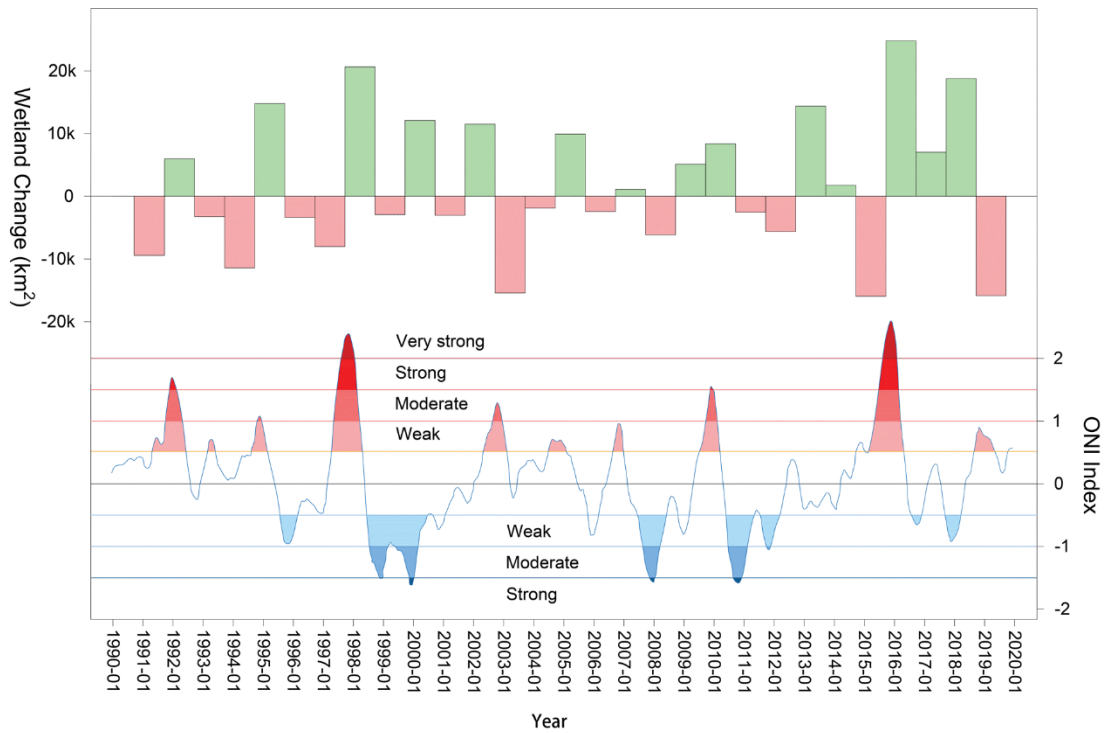
1
2 **Fig. S2.** The spatial distributions of the transitional and unstable type of permafrost
3 and new wetlands. The overlapping regions are shown in blue. Permafrost data was
4 obtained from Ran et al. (2020). It is drawn on the standard map (Map No. : GS 京
5 (2023)0108) from the Standard Map Service System of the Ministry of Natural
6 Resources.

7
8



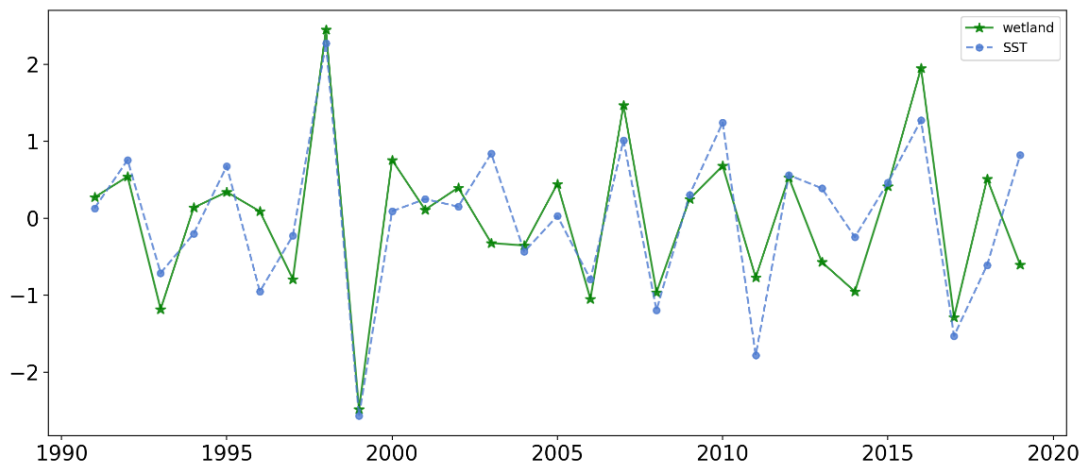
9
10 **Fig. S3.** Relationships of the wetland areal extent, lake areal extent and lake number on
11 the source region of the Yangtze River and Qiangtang Plateau.

12
13



1
2
3
4
5
6
7

Fig. S4. Interannual variations of TP wetland areal extent linked to Oceanic Niño Index (ONI). In the upper panel, each of the bar charts shows the TP wetland area change compared with the previous year. In the lower panel, the red and blue areas represent El Niño and La Niña at different levels, respectively.



8
9
10
11
12
13

Fig. S5. The first SVD mode of time series of the wetland areal extent and SST.

1 Tables

2
3 **Table S1.** Statistical results of the wetland areal extent and climate variables in TP

Method	Qiangtang Plateau		Source Region of Yangtze River		Qaidam Basin		
	Variable	r	p	r	P	r	p
	AT	0.880	2.9e-9*	0.841	0.001*	0.628	5.7e-5*
CA	AP	0.517	6.8e-3*	0.529	0.004*	0.685	3.4e-4*
	APE	0.319	0.09	0.403	0.032	0.567	1.6e-3*
	Variable	MS	SS, %	MS	SS, %	MS	SS, %
GLM	AT	1682.9	54.5	40.63	62.0	8.48	17.3
	AP	1356.1	43.9	23.82	36.4	32.96	67.3
	APE	28.7	0.9	0.18	0.3	6.75	13.8
	Residuals	22.4	0.7	0.86	1.3	0.80	1.6

4 r, Pearson correlation coefficient; * for $p < 0.05$. CA, correlation analysis. GLM,
5 general linear model. SS, proportion of variances explained by the variable. MS, mean
6 squares.

7
8 **Table S2.** The variance contribution rates of the first five modes from SVD between
9 the SST with the wetland areal extents on the TP

SVD mode	1	2	3
variance contribution	0.420	0.118	0.109
cumulative variance contribution	0.420	0.538	0.647
correlation coefficient	0.812	0.862	0.777

10 References

- 11 [1] Chen J, Zhu X, Vogelmann JE, Gao F, Jin S. A simple and effective method for filling gaps in
12 Landsat ETM+ SLC-off images. *Remote Sensing of Environment* 2011;115:1053–64.
- 13 [2] Martens B, Miralles DG, Lievens H, Van Der Schalie R, De Jeu RA, Fernández-Prieto D, et
14 al. GLEAM v3: Satellite-based land evaporation and root-zone soil moisture. *Geoscientific
15 Model Development* 2017;10:1903–25.

- 1 [3] Miralles DG, Holmes T, De Jeu R, Gash J, Meesters A, Dolman A. Global land-surface
2 evaporation estimated from satellite-based observations. *Hydrology and Earth System*
3 *Sciences* 2011;15:453–69.
- 4 [4] Mao D, Wang Z, Du B, Li L, Tian Y, Jia M, et al. National wetland mapping in China: A new
5 product resulting from object-based and hierarchical classification of Landsat 8 OLI images.
6 *ISPRS Journal of Photogrammetry and Remote Sensing* 2020;164:11–25.
- 7 [5] Lang Q, Niu Z, Hong X, Yang X. Remote Sensing Monitoring and Change Analysis of
8 Wetlands in the Tibetan Plateau. *Geomatics and Information Science of Wuhan University*,
9 2021; 46:230-237.
- 10 [6] Feng S, Liu S, Huang Z, Jing L, Zhao M, Peng X, et al. Inland water bodies in China: Features
11 discovered in the long-term satellite data. *Proceedings of the National Academy of Sciences*
12 2019;116:25491–6.
- 13 [7] Sun C, Shrivastava A, Singh S, Gupta A. Revisiting unreasonable effectiveness of data in deep
14 learning era. *Proceedings of the IEEE international conference on computer vision*, 2017, p.
15 843–52.
- 16 [8] Pekel J-F, Cottam A, Gorelick N, Belward AS. High-resolution mapping of global surface
17 water and its long-term changes. *Nature* 2016; 540:418–22.
- 18 [9] Kaiser P, Wegner JD, Lucchi A, Jaggi M, Hofmann T, Schindler K. Learning Aerial Image
19 Segmentation From Online Maps. *IEEE Trans Geosci Remote Sensing* 2017;55:6054–68.
- 20 [10] Kemker R, Salvaggio C, Kanan C. Algorithms for semantic segmentation of multispectral
21 remote sensing imagery using deep learning. *ISPRS Journal of Photogrammetry and Remote*
22 *Sensing* 2018;145: 60–77.
- 23 [11] Hu J, Shen L, Sun G. Squeeze-and-Excitation Networks. *Proceedings of the IEEE Computer*
24 *Society Conference on Computer Vision and Pattern Recognition* 2018:7132–41.
- 25 [12] Stehman SV, Foody GM. Key issues in rigorous accuracy assessment of land cover products.
26 *Remote Sensing of Environment* 2019;231:111199.
- 27 [13] Olofsson P, Foody GM, Stehman SV, Woodcock CE. Making better use of accuracy data in
28 land change studies: Estimating accuracy and area and quantifying uncertainty using stratified
29 estimation. *Remote Sensing of Environment* 2013;129:122–31.
- 30 [14] Tao S, Fang J, Zhao X, Zhao S, Shen H, Hu H, et al. Rapid loss of lakes on the Mongolian
31 Plateau Supporting Texts Text S1 . Short descriptions on 13 Ramsar sites located on the
32 Mongolian Plateau. *Proceedings of the National Academy of Sciences* 2015;112:2281–6.
- 33 [15] Bretherton CS, Smith C, Wallace JM. An Intercomparison of Methods for Finding Coupled
34 Patterns in Climate Data. *Journal of Climate* 1992;5:541–60.
- 35